KYBERNETIKA — VOLUME *45* (2009), NUMBER 4, PAGES 657 – 669

IMPLEMENTATION OF THE MR TRACTOGRAPHY VISUALIZATION KIT BASED ON THE ANISOTROPIC ALLEN–CAHN EQUATION

Pavel Strachota

Magnetic Resonance Diffusion Tensor Imaging (MR–DTI) is a noninvasive in vivo method capable of examining the structure of human brain, providing information about the position and orientation of the neural tracts. After a short introduction to the principles of MR–DTI, this paper describes the steps of the proposed neural tract visualization technique based on the DTI data. The cornerstone of the algorithm is a texture diffusion procedure modeled mathematically by the problem for the Allen–Cahn equation with diffusion anisotropy controlled by a tensor field. Focus is put on the issues of the numerical solution of the given problem, using the finite volume method for spatial domain discretization. Several numerical schemes are compared with the aim of reducing the artificial (numerical) isotropic diffusion. The remaining steps of the algorithm are commented on as well, including the acquisition of the tensor field before the actual computation begins and the postprocessing used to obtain the final images. Finally, the visualization results are presented.

Keywords: Allen–Cahn equation, anisotropic diffusion, finite volume method, MR–DTI, MR tractography, medical visualization

AMS Subject Classification: 93E12, 62A10, 62F15

1. INTRODUCTION TO MR–DTI

Modern magnetic resonance (MR) systems used in medicine have become versatile noninvasive diagnostic tools. Thanks to the wide capabilities of configuration of the signal acquisition sequences, many different *Magnetic Resonance Imaging* (MRI) methods aimed at examining different parts of human body have been developed. The MR-DTI (*Diffusion Tensor Imaging*, [4]) technique allows the MR scanner to examine anisotropic structures in tissues, such as heart muscle fibers or neural tracts in the brain [6]. The principle of this method is summarized in the following paragraphs.

Physical background of MRI

The hardware of a MR scanner consists of the following components:

- A strong magnet generating a static primary magnetic field B_0, as homogeneous as possible. There exist devices utilizing permanent magnets, electromagnets (resistive magnets), and superconducting coils. Only the last type is suitable for MR–DTI.
- *Shim coils* being part of the hardware subsystem designated for improving the homogeneity of B_0.
- *Gradient coils* able to temporarily introduce secondary magnetic field gradients aligned along the axes of the machine's intrinsic coordinate system. As a combination of these, a magnetic field gradient can be generated along an arbitrary direction in space. Among other purposes, gradient coils are crucial for spatial encoding of the MR signal.
- *Radio frequency* (RF) *coil* responsible for actions leading to MR signal generation and also used for signal measurement.
- Other components including various types of measurement coils mounted to patient's body, coil cooling systems, control systems, bed adjustment mechanisms etc.

The most common examination method is focused on the ${}^1_1\mathrm{H}$ nuclei (i. e. single protons) contained in abundance within all soft tissues of human body, mainly as part of H_2O molecules [5, 11]. Their angular momentum (spin) generates *magnetic moment*. When the patient enters the MR scanner, the proton spins begin to precess around the direction of B_0, i. e. the direction along the bore of the coil, usually referred to as the z axis. The precession occurs at the *Larmor frequency* [5]

$$\omega = \gamma B_0,$$

where γ is the *gyromagnetic ratio*, a constant specific to the ${}^1_1\mathrm{H}$ nucleus. The *net magnetization*, i. e. the vector sum of magnetic moments of the individual protons in some macroscopic volume, becomes nonzero and aligns with the field B_0, as the distribution of the spin precession phase is uniform.

Afterwards, a sequence of pulses is applied in order to generate the MR signal, to measure it subsequently, and to locate its origin in space. For the sake of simplicity, one can consider only the following parts of the sequence; for details, we refer the reader again to [5, 11] and to [19].

- The z-oriented gradient is turned on, making the Larmor frequency depend on the z coordinate, i. e. $\omega = \omega(z)$. At the same time, the RF electromagnetic pulse is applied, with a spectrum spanning a narrow neighborhood of some frequency ω_{RF}. Due to resonance, only the protons satisfying $\omega(z) \approx \omega_{\mathrm{RF}}$ are influenced, which is the principle of *slice selection*. In the affected layer, the proton precession is synchronized, causing the net magnetization to precess

around the z axis. Its longitudinal component (parallel with z) is reduced or canceled due to flipping of the proton magnetic moment orientations [5].

- After the RF pulse vanishes, the net magnetization gradually relaxes to equilibrium. During this period, the *MR signal*, i. e. the electric current induced by net magnetization precession, can be detected in the measurement coil(s).
- Before the actual measurement, a short pulse of magnetic field gradient along one of the remaining axes (WLOG denoted by y) is imposed on the tissue, creating a phase shift of the net magnetization precession along y.
- The gradient along x is turned on and at the same time, the measurement of the signal sample is performed. As the magnetic field gradient also triggers the gradient of Larmor frequency along x, a Fourier transform of the signal sample can be used to obtain spatial distribution of the MR signal strength along x (*frequency encoding*).

Layer selection together with frequency encoding and repeated measurements with different phase shifts (*phase encoding*) finally provide a complete MR signal image on a 3D spatial grid. Its typical resolution is 128 or 256 volume elements (*voxels*) in the x, y directions, with the diameter of the voxel around 1–4 mm. The resolution in the z direction can be lower, depending on the thickness of the slice.

Extension to DWI

The particular MRI techniques differ among other aspects in the additional steps of the acquisition procedure and in the interpretation of either the MR signal strength or the relaxation time. DWI (*Diffusion Weighted Imaging*) adds the following steps between the RF pulse and the measurement itself [14, 17].

1. A "*dephase*" pulse of magnetic field gradient in a selected direction is imposed on the tissue. Again, this leads to a phase shift and disrupts the synchronicity of the proton spin precession.
2. After a short period, a "*rephase*" pulse of an inverse gradient is applied, restoring the synchronicity of spin precession in H_2O molecules that *have not moved*.

In molecules that *have moved* along the gradient direction due to diffusion (i. e. Brownian motion), the precession cannot be resynchronized this way. That results in a measurable MR signal loss, proportional to the water diffusion strength in the direction of the applied gradient. The signal loss can be compared with the reference image obtained without the dephase-rephase sequence to get a *diffusion weighted image*.

DTI and the diffusion tensor field

Denote by Ω_0 the examined volume of the brain. The purpose of DTI is to measure the strength and directional distribution of water molecule diffusion in each voxel

$\boldsymbol{x} \in \Omega_0$ and encode the information into a *diffusion tensor field*. Performing series of DWI measurements with different gradient directions allows us to assemble $\forall\, \boldsymbol{x} \in \Omega_0$ a system of Stejskal–Tanner equations [20, 22] for the elements of the symmetric positive definite diffusion tensor $\boldsymbol{D}(\boldsymbol{x}) \in \mathbb{R}^{3\times 3}$. Six equations are the necessary minimum, however, using more gradient directions together with some estimation method (such as least squares) for the resulting overdetermined equation system, one can obtain a more robust calculation of $\boldsymbol{D}(\boldsymbol{x})$. There exist MR scanners capable of measuring over 200 different directions, whose optimal choice is a matter of ongoing research (e. g. [9]).

The diffusion tensor is a second order approximation of the directional distribution of water diffusion strength at the given point $\boldsymbol{x}$. It can be interpreted by the *diffusion ellipsoid* defined as

$$\Gamma(\boldsymbol{x}) = \left\{ \boldsymbol{\eta} \in \mathbb{R}^3 \,\middle|\, \boldsymbol{\eta}^T \boldsymbol{D}(\boldsymbol{x})^{-1} \boldsymbol{\eta} = 1 \right\}.$$

The diffusion strength along the vector $\boldsymbol{v}$ is proportional to the distance from the origin to $\Gamma(\boldsymbol{x})$ in the direction of $\boldsymbol{v}$ and the eigenvalues of $\boldsymbol{D}(\boldsymbol{x})$ represent the lengths of the principal axes of $\Gamma(\boldsymbol{x})$.

It has been observed that diffusion prevails in the direction parallel to the neural fiber tracts [4]. Hence, it is possible to perform MR *tractography*, i. e. to reconstruct a model of the fiber bundles by following the pathways of the strongest diffusion.

2. OVERVIEW OF THE PROPOSED VISUALIZATION ALGORITHM

Principle of the method

There are several approaches to the realization of the tractography procedure (see e. g. [8, 22]). We have elaborated an algorithm based on imitating the diffusion processes taking place in the brain tissue, similar to the technique introduced in [21]. The idea is to apply an anisotropic diffusion process [18] to a noisy 3D texture contained in the domain $\Omega \subset \Omega_0$, representing the chosen *region of interest* (ROI). The anisotropy of the diffusion is controlled by the tensor field $\boldsymbol{D}$ so that the distribution of the texture diffusion strength corresponds to the physical process measured in the brain. As a result, the initial noisy image is smeared in such a way that the streamlines of the tensor field become distinguishable. The 3D volume Ω can then be sliced to produce human readable planar images.

The described steps have been implemented in the MEGIDDO (Medical Employment of Generating Images by Degenerate Diffusion Operator) software kit. In the following paragraphs, we will focus on the details of its data processing workflow (see Figure 1).

Data acquisition

Raw DWI datasets are delivered from the scanner either in a proprietary format used for the vendor supplied software or in the well documented ANALYZE 7.5 or DICOM formats. Currently, the DTI module of MedINRIA (developed within the

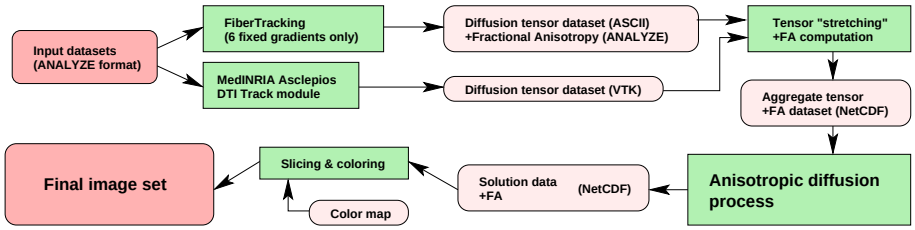

Fig. 1. MEGIDDO data processing workflow.

ASCLEPIOS project at INRIA, Sophia Antipolis, France) is used to process these images and to compute the diffusion tensor field, which may also involve thresholding and smoothing to cope with noise in the input data [20]. Alternatively, one can use the FiberTracking utility [8], which is limited to 6 gradient directions only.

Fractional anisotropy and diffusion ellipsoid stretching

Denote by $\lambda_1 \geq \lambda_2 \geq \lambda_3$ the eigenvalues of $\boldsymbol{D}(\boldsymbol{x})$ for some $\boldsymbol{x} \in \Omega$ and let $\boldsymbol{v}_i$ represent the eigenvector corresponding to λ_i. The diffusion strength therefore assumes its maximum in the direction of $\boldsymbol{v}_1$ and is proportional to λ_1. Hence, $\boldsymbol{v}_1$ may also represent the tangential direction of the possible neural tract at the point $\boldsymbol{x}$. The number of neural fibers actually present at this location may be considered proportional to the anisotropy strength, which is quantified by the *fractional anisotropy* (FA, see e. g. [4]) defined as

$$FA = \frac{\sqrt{3\left((\lambda_1 - \lambda)^2 + (\lambda_2 - \lambda)^2 + (\lambda_3 - \lambda)^2\right)}}{\sqrt{2\left(\lambda_1^2 + \lambda_2^2 + \lambda_3^2\right)}}, \tag{1}$$

where

$$\lambda = \frac{1}{3}\left(\lambda_1 + \lambda_2 + \lambda_3\right).$$

It is easy to verify that $FA \in [0, 1)$, where 0 indicates perfect isotropy (one should not expect any anisotropic structures, i. e. fibers, at the point $\boldsymbol{x}$) and 1 would mean perfect anisotropy ($\lambda_2 = \lambda_3 = 0$, Γ degenerates to a line segment). Generally, the greater the value of FA, the more neural fibers are present. However, the converse does not hold: As the diffusion ellipsoid is a quadric surface, it cannot represent the focusing of anisotropy to more than one main direction (e. g. fiber bundle crossing). In such a case, FA would approach zero.

Even though the idea was to use the original tensor field $\boldsymbol{D}$ for the visualization process, the anisotropy strength described by $\boldsymbol{D}$ has proved to be too weak to produce observable streamlines. To overcome this difficulty, a preprocessing utility has been created to modify $\boldsymbol{D}$ so that the corresponding diffusion ellipsoids are stretched along their largest principal axis. For each voxel $\boldsymbol{x}$, the positive eigenvalues

λ_i are calculated by an explicit formula for finding the roots of the characteristic polynomial of $\boldsymbol{D}(\boldsymbol{x})$, operating in $\mathbb{R}$. Afterwards, the symmetry of $\boldsymbol{D}(\boldsymbol{x})$ is used with advantage to find an orthonormal set of eigenvectors $\boldsymbol{v}_i$. The fractional anisotropy and the modified tensor field $\tilde{\boldsymbol{D}}$ are then computed and saved together to a single NetCDF dataset.

Anisotropic diffusion by the Allen–Cahn equation

When the tensor field is ready, the actual visualization phase takes place. Generally, the diffusion process found in various contexts can be described by a mathematical model formulated as a problem for a partial differential equation with a diffusion term (see e. g. [3, 13]). For the purposes of the proposed algorithm, the Allen–Cahn equation [2] has been chosen.

Consider the time interval $\mathcal{J} = (0, T)$, the domain $\Omega \subset \mathbb{R}^3$ in the form of a block and the diffusion tensor field $\tilde{\boldsymbol{D}} : \bar{\Omega} \mapsto \mathbb{R}^{3\times 3}$ representing the input data. The initial boundary value problem for the Allen–Cahn diffusion equation reads

$$\xi \frac{\partial p}{\partial t} = \xi \nabla \cdot \tilde{\boldsymbol{D}} \nabla p + \frac{1}{\xi} f_0(p) \qquad \text{in } \mathcal{J} \times \Omega, \tag{2}$$

$$\left.\frac{\partial p}{\partial n}\right|_{\partial\Omega} = 0 \qquad \text{on } \mathcal{J} \times \partial\Omega, \tag{3}$$

$$p|_{t=0} = I \qquad \text{in } \Omega, \tag{4}$$

where p is the unknown function $p : \bar{\mathcal{J}} \times \bar{\Omega} \to \mathbb{R}$ interpreted as the texture intensity, I represents a noisy initial condition, $f_0(p) = p(1-p)\left(p - \frac{1}{2}\right)$, and $\xi > 0$ is a small parameter related to the thickness of the diffusion interface layer [1].

The problem (2) – (4) is solved numerically on a structured rectangular grid, which will be discussed in more detail in the next section. In principle, the procedure consists of the following steps:

1. The tensor field is interpolated from the original voxel grid onto the computation grid, which is finer in order to achieve greater resolution of the resulting streamlines. In particular, trilinear element wise interpolation is employed. This causes a change of shape of the corresponding diffusion ellipsoid along the way from one voxel to another. As shown in [17], more complex forms of interpolation might be preferred in some cases, so that only the orientation is changed, but the shape is maintained. More precisely, the fractional anisotropy as the function $FA : \Omega \to [0, 1)$ is supposed to satisfy

$$\min_{\boldsymbol{t}\in[\boldsymbol{x},\boldsymbol{y}]} FA(\boldsymbol{t}) = \min\{FA(\boldsymbol{x}), FA(\boldsymbol{y})\},$$

   where $[\boldsymbol{x}, \boldsymbol{y}]$ is the line segment connecting the neighboring voxels at positions $\boldsymbol{x}$, $\boldsymbol{y}$.

2. The initial condition containing random impulse noise is generated on the computational grid.

3. The numerical solution of the given problem is found. The solution is a function of both space and time and its value at some final time $T > 0$ is considered the visualization result. The most suitable setting of T is estimated by experiment.

Colorization and slicing

After the diffusion process is completed, the postprocessing phase begins, which involves slicing and colorization. The 3D grid is divided into slices cut in one of the principal planes of the human body: *transverse*, *sagittal*, or *coronal* plane [10]. These planar grayscale images are then colorized by multiplying the brightness of each pixel by the color representation of FA at the corresponding voxel of the domain Ω_0 (see Figure 6). The color is obtained by using a linear function mapping the interval

$$\left[0, \max_{\boldsymbol{x}\in\Omega_0} FA\left(\boldsymbol{x}\right)\right]$$

onto the color scale. The NetCDF dataset produced by performing the diffusion process can be reused to generate several sets of slices.

3. NUMERICAL SOLUTION OF THE PROBLEM FOR THE ALLEN–CAHN EQUATION

For numerical solution of the problem (2) – (4), the *method of lines* is used [15, 16], allowing to separate the steps of temporal and spatial discretization and to choose an arbitrary suitable technique for each of them:

- Temporal discretization is carried out by the 4th order Runge–Kutta–Merson method with adaptive time stepping, which automates the time step adjustment so that it always satisfies the stability condition of the numerical scheme.
- For spatial discretization, the finite volume (FV) method [7] on a rectangular structured grid is employed.

The latter step yields a semidiscrete scheme in the form

$$\xi \frac{\mathrm{d}}{\mathrm{d}t} p_K\left(t\right) = \xi \sum_{\sigma\in\mathcal{E}_K} F_{K,\sigma}\left(t\right) + \frac{1}{\xi} f_{0,K}\left(t\right),$$

where $\mathcal{E}_K$ is the set of all faces of the cell K. $F_{K,\sigma}\left(t\right)$ are the respective numerical fluxes at the time t, which contain higher order difference quotients observing a symmetric 5-point stencil and approximating the derivatives $\partial_x p$, $\partial_y p$, $\partial_z p$ at the center of the face σ.

- The difference quotient approximating the derivative in the direction perpendicular to the face σ uses a non-equidistant point distribution in order to prevent redundant interpolation (Figure 2 a).
- The remaining derivatives are approximated using a uniform 5-point stencil. The stencil points (the crosses along the dashed line in Figure 2 b) are interpolated from the neighboring grid nodes using 1-dimensional cubic interpolation.

The choice of the higher order scheme is justified in the following paragraph.

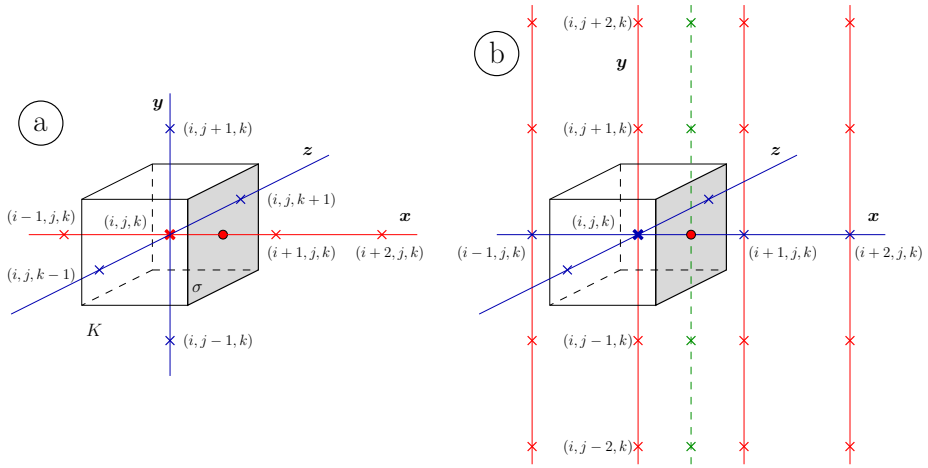

Fig. 2. Difference quotients in derivative approximations.

Artificial diffusion

The resulting streamline visualization is expected to form fine high frequency structures with steep gradients in the direction perpendicular to the streamlines, spanning a small number of grid nodes. However, the numerical scheme distorts this behavior of the solution by introducing undesired artificial (numerical) isotropic diffusion. By means of Fourier error analysis [12], the number of *grid points per wave* (PPW) can be estimated for a given difference operator. Depending on the spectrum of the solution, this quantity defines the grid density necessary to produce an approximation error below the desired level. As PPW decreases significantly with the order of the difference operator, we obtain two general possibilities of artificial diffusion reduction: increasing the order of approximation and/or refining the grid. However, due to the CPU and memory requirements of the computation on a 3D grid, the latter is not an option.

The comparison of four different schemes restricted to $\mathbb{R}^2$ is shown in Figure 3. In both cases, the initial condition depicted on the very left underwent a process of anisotropic diffusion directed along the axis $y = x$. The results achieved by the respective schemes are ordered with respect to the increasing effect of artificial isotropic diffusion. The first result corresponds to the scheme described above.

Parallelization

In order to allow visualization of the whole brain at once at high resolution, the numerical algorithm has been parallelized. As the target platform, any UNIX cluster (i. e. distributed memory architecture) supporting the MPI library for message passing can be used. At the moment, the grid is decomposed into simple slices along the y axis (with respect to input dataset ordering), making it possible to utilize an

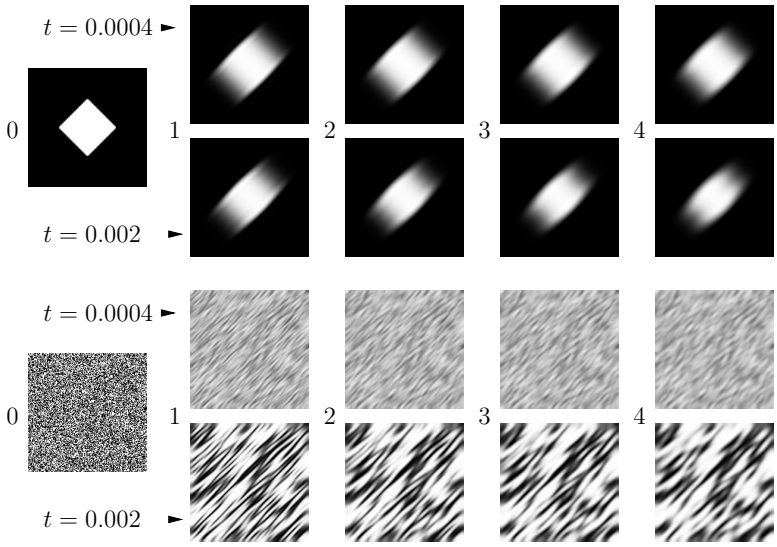

0. Initial condition

1. FV, 5-point (4th order), cubic interpolation

2. FV, 5-point, linear interpolation

3. FV, 2nd order central difference

4. Finite difference, 1st order forward-backward

Fig. 3. Artificial diffusion in different numerical schemes, 2 time levels.

arbitrary number of processes for the computation. The EOC analysis discussed below as well as the results presented in the last section have been obtained using the IBM Cluster 1350 and the IBM Bladecenter LS21 systems at the CINECA high performance computing center in Bologna, Italy (see *Acknowledgments*).

Convergence

Experimental order of convergence (EOC) has been measured for the higher order FV scheme with cubic interpolation. EOC is obtained by computing the solution on a sequence of gradually refining grids ($\mathcal{T}_i$) and is defined as

$$\mathrm{EOC}_i = \log\left(\frac{\mathrm{Error}_i}{\mathrm{Error}_{i-1}}\right) \Big/ \log\left(\frac{h_i}{h_{i-1}}\right),$$

where $h_i = \max_{K\in\mathcal{T}_i} \operatorname{diam}(K)$ is the mesh size and Error_i is the difference of the ith solution from the precise solution measured in an appropriate norm. As the precise solution is not known, it has been replaced by the numerical solution on a very fine mesh. The results confirming the convergence together with the computational details are summarized in Table 1.

Table 1. EOC results for the higher order finite volume scheme.
Computational domain $\Omega = (0,1) \times (0,1) \times \left(0, \frac{1}{2}\right)$.
Precise solution replaced by numerical solution using $h = 1.276 \times 10^{-3}$,
consuming 44 min of wall time on 80 cores of the IBM Bladecenter LS21.

h	$L_\infty(\mathcal{J}; L_2(\Omega))$ error	EOC in $L_\infty(\mathcal{J}; L_2(\Omega))$	$L_\infty(\mathcal{J}; L_\infty(\Omega))$ error	EOC in $L_\infty(\mathcal{J}; L_\infty(\Omega))$
1.020E-02	1.806E-04	–	3.798E-03	–
5.102E-03	6.137E-05	1.557E+00	1.188E-03	1.675E+00
2.551E-03	1.828E-05	1.747E+00	5.256E-04	1.177E+00

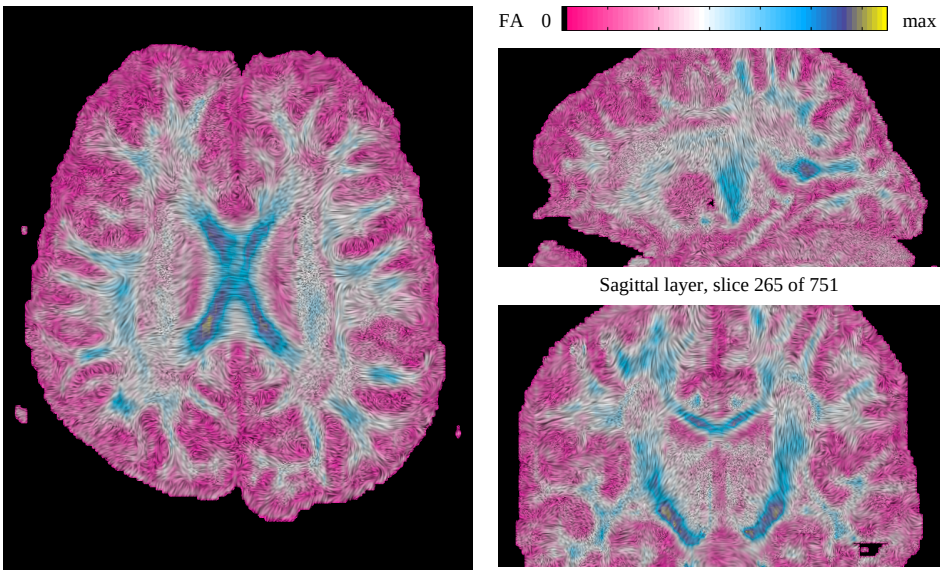

Fig. 4. Slices of the DTI complete brain visualization, examination of a healthy volunteer. Dataset dimensions: $900 \times 751 \times 445$ voxels.

4. VISUALIZATION RESULTS

In Figures 4 and 5, we demonstrate the function of the MEGIDDO visualization kit on two sample input datasets. The streamlines of the tensor field indicate the location and direction of the neural tracts. Colorization by the value of fractional anisotropy FA is obtained by performing the color mapping procedure depicted schematically in Figure 6 and explained in detail in the last paragraph of Section 2.

The source diffusion tensor field for images in Figure 4 has been acquired by 7 DWI examinations of a healthy volunteer with the standard encoding of 6 gradi-

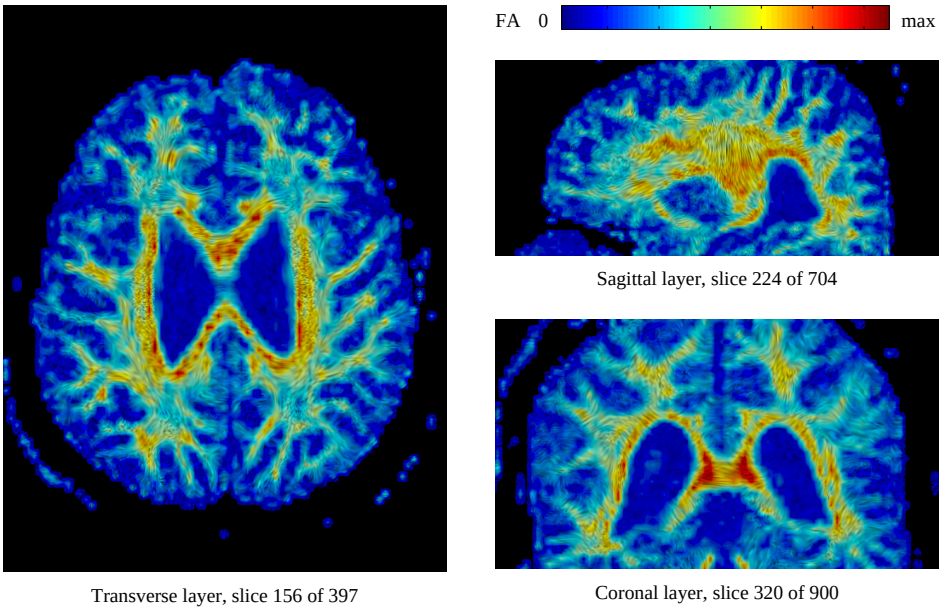

Fig. 5. Slices of the DTI complete brain visualization, examination of a patient. Dataset dimensions: $900 \times 704 \times 397$ voxels.

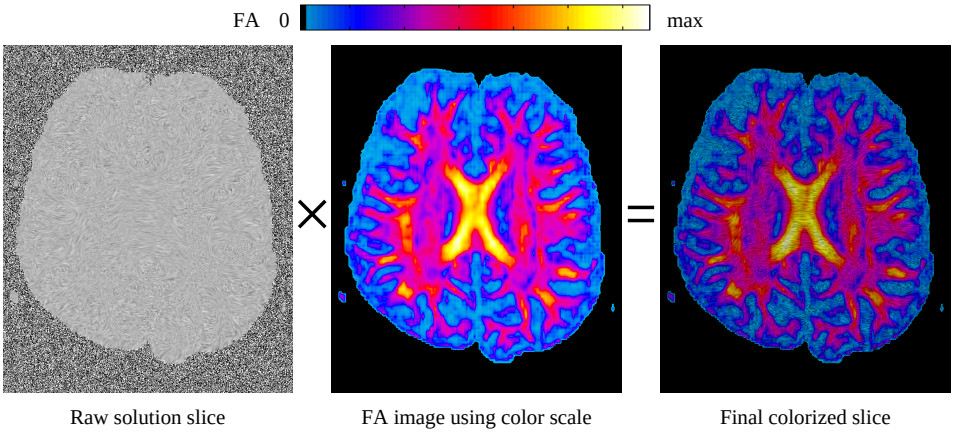

Fig. 6. Colorization of the raw result of the visualization process.

ent directions [22]. The second dataset has been obtained from 20 measurements with different gradient directions, performed by a modern 3T scanner at IKEM, Prague. The resulting tractography in Figure 5 depicts pathological morphology in

the patient's cerebrum.

In terms of computational resources, the visualizations in Figures 4, 5 are feasible on 16 cores of AMD Opteron 2.4 GHz within less than 100 min, using approximately 20GiB of memory.

5. CONCLUSION

We present a fully functional implementation of the DTI visualization procedure based on anisotropic diffusion of a noisy texture. This approach may represent a suitable complement to the established tractography techniques utilizing explicit fiber tracking algorithms. While these methods usually require the user to specify starting and ending ROI [8] so that they can find the likely connections between them, our approach provides a global overview of the fiber tract structure in the whole brain or in the specified region. The main drawback of the current algorithm are its extensive resource demands in terms of memory and CPU time. Further efforts should therefore be focused on optimization of the numerical algorithm and on finding possibilities of incorporating the visualization results into some medical viewer software.

ACKNOWLEDGMENT

This work was carried out under the HPC-EUROPA++ project (project number: 211437), with the support of the European Community – Research Infrastructure Action of the FP7 "Coordination and support action" Program. Partial support of the project "Jindřich Nečas Center for Mathematical Modeling", No. LC06052. Special thanks to the colleagues at the Institute for Clinical and Experimental Medicine (IKEM) in Prague for providing input datasets, consultations, and support.

(Received October 30, 2008.)

REFERENCES

[1] M. Beneš: Mathematical analysis of phase-field equations with numerically efficient coupling terms. Interfaces and Free Boundaries *3* (2001), 201–221.

[2] M. Beneš: Diffuse-interface treatment of the anisotropic mean-curvature flow. Appl. Math. *48* (2003), 6, 437–453.

[3] M. Beneš, V. Chalupecký, and K. Mikula: Geometrical image segmentation by the Allen–Cahn equation. Appl. Numer. Math. *52* (2004), 2, 187–205.

[4] D. L. Bihan et al.: Diffusion tensor imaging: Concepts and applications. J. Magnetic Resonance Imaging *13* (2001), 534–546.

[5] W. F. Block et al.: Encyclopedia of Medical Devices and Instrumentation, chapter Magnetic Resonance Imaging. Second edition. Wiley, New York 2006, pp. 283–298.

[6] A. F. M. Dasilva et al.: A primer on diffusion tensor imaging of anatomical substructures. Neurosurgical Focus *15* (2003), 1–4.

[7] R. Eymard, T. Gallouët, and R. Herbin: Finite volume methods. In: Handbook of Numerical Analysis (P. G. Ciarlet and J. L. Lions, eds.), volume 7, Elsevier, 2000, pp. 715–1022.

[8] P. Fillard and G. Gerig: Analysis tool for diffusion tensor MRI. In: Proc. Medical Image Computing and Computer-Assisted Intervention (MICCAI), Springer–Verlag, Berlin 2003, pp. 967–968.

[9] K. M. Hasan, D. L. Parker, and A. L. Alexander: Comparison of gradient encoding schemes for diffusion-tensor MRI. J. Magnetic Resonance Imaging *13* (2001), 769–780.

[10] W. Kahle, H. Leonhardt, and W. Platzer: Color Atlas and Textbook of Human Anatomy in 3 Volumes, volume 1: Locomotor System. Third edition. Georg Thieme Verlag, Stuttgart 1986.

[11] Z.-P. Liang and P. C. Lauterbur: Principles of Magnetic Resonance Imaging: A Signal Processing Perspective. Wiley–IEEE Press, 1999.

[12] H. Lomax, T. H. Pulliam, and D. W. Zingg: Fundamentals of Computational Fluid Dynamics. Springer–Verlag, Berlin 2001.

[13] J. Mach: Application of non-linear diffusion in algorithms of mathematical visualization. In: Proc. Czech–Japanese Seminar in Applied Mathematics 2006 (M. Beneš, M. Kimura, and T. Nakaki, eds.), volume 6 of COE Lecture Note, Faculty of Mathematics, Kyushu University Fukuoka, 2007, pp. 156–164.

[14] S. Mori and J. Zhang: Principles of diffusion tensor imaging and its applications to basic neuroscience research. Neuron *51* (2006), 527–539.

[15] T. Oberhuber: Finite difference scheme for the Willmore flow of graphs. Kybernetika *43* (2007), 6, 855–867.

[16] W. E. Schiesser: The Numerical Method of Lines: Integration of Partial Differential Equations. Academic Press, San Diego 1991.

[17] R. Sierra: Nonrigid Registration of Diffusion Tensor Images. Master's Thesis, Swiss Federal Institute of Technology, Zurich 2001.

[18] P. Strachota: Anisotropic Diffusion in Mathematical Visualization. In: Science and Supercomputing in Europe – Report 2007, Bologna 2008, CINECA Consorzio Interuniversitario, pp. 826–831,

[19] J. S. Suri, S. K. Setarehdan, and S. Singh, eds.: Advanced Algorithmic Approaches to Medical Image Segmentation: State-of-the-art Application in Cardiology, Neurology, Mammography and Pathology. Springer–Verlag, New York 2002.

[20] D. Tschumperlé and R. Deriche: Variational frameworks for DT-MRI estimation, regularization and visualization. In: Ninth IEEE Internat. Conference on Computer Vision (ICCV'03), volume 1, 2003, p. 116.

[21] D. Tschumperlé and R. Deriche: Tensor Field Visualization with PDE's and Application to DT-MRI Fiber Visualization. INRIA Sophia-Antipolis, Odyssée Lab. 2004.

[22] C. F. Westin et al.: Processing and visualization for diffusion tensor MRI. Medical Image Analysis *6* (2002), 93–108.

Pavel Strachota, Department of Mathematics, Faculty of Nuclear Sciences and Physical Engineering, Czech Technical University in Prague, Trojanova 13, 120 00 Praha 2. Czech Republic.
pavel.strachota@fjfi.cvut.cz